electronics

MDPI

Article

Application of deep neural network to the reconstruction of two-phase material imaging by capacitively coupled electrical resistance tomography

Zhuoran Chen [1]+, Gege Ma [1]+, Yandan Jiang [2], Baoliang Wang [2] and Manuchehr Soleimani [1,*]

[1] Engineering Tomography Laboratory (ETL), Department of Electronic and Electrical Engineering, University of Bath, Bath, UK
[2] State Key Laboratory of Industrial Control Technology, College of Control Science and Engineering, Zhejiang University, Hangzhou, China
* Correspondence: M.Soleimani@bath.ac.uk, + The first two authors are both first author.

Abstract: A convolutional neural network (CNN) based image reconstruction algorithm for two-phase material imaging is presented and verified with experimental data from capacitively coupled electrical resistance tomography (CCERT) sensor. As a contactless version of electrical resistance tomography (ERT), CCERT has advantages such as no invasion, low cost, no radiation, rapid response for two-phase material imaging. Besides, CCERT avoids contact error of ERT by imaging from outside of the pipe. Forward modelling was implemented based on the practical circular array sensor, and the inverse image reconstruction was realized by CNN-based supervised learning algorithm as well as the well-known total variation (TV) regularization algorithm for comparison. The 2D monochrome 2500-pixel image was divided into 625 clusters, and each cluster was used individually to train its own CNN to solve the 16-classes classification problem. Inherent regularization for assumption of binary materials enabled us to use a classification algorithm with CNN. The iterative TV regularization algorithm achieved a close state of the two-phase material reconstruction by its sparsity-based assumption. The supervised learning algorithm established the mathematical model that maps the simulated resistance measurement to the pixel patterns of clusters. The training process was carried out only using simulating measurement data, but simulating and experimental tests were both conducted to investigate the feasibility of applying multiple-layers CNN for CCERT imaging. The performance of CNN algorithm on simulated data is demonstrated, and the comparison between the results created by the TV-based algorithm and the proposed CNN algorithm with the real-world data is also provided.

Keywords: convolutional neural network (CNN); supervised deep learning; capacitively coupled electrical resistance tomography (CCERT); image reconstruction

Citation: Lastname, F.; Lastname, F.; Lastname, F. Title. *Electronics* **2021**, *10*, x. https://doi.org/10.3390/xxxxx

Academic Editor: Firstname Lastname

Received: 9 March 2021
Accepted: date
Published: date

1. Introduction

Electrical impedance tomography (EIT) has been studied and widely applied in medical imaging and process tomography since it was raised in the 1980s [1-5]. The conductivity distribution within the target region, such as areas of the human body or the contents of pipeline and vessel, can be revealed based on the impedance measurements via electrodes placed on the boundary of the region [6]. Compared to other imaging protocols, EIT has the advantages of producing images with high temporal resolution while having a relatively low cost, no radiation, no invasion, rapid response, and simplicity for application [6,7]. In late 1980s when EIT was introduced to the process tomography field, electrical resistance tomography (ERT), a particular case of EIT, was proposed [8,9]. Compared with EIT, it has similar imaging processes except that the phase angle of the

detected impedance is omitted so that the images are reconstructed merely by the resistance [8].

However, direct contact between the electrodes and conductive medium in traditional ERT causes problems. ERT images are sensitive to electrode properties, for example, contact impedance [10]. In medical application, the high-value contact impedance would vary with body movement and studied areas [11]. Besides, it is sensitive to the nature of the contact layer, thus, the lack of boundary properties in clinical experiments could lead to inaccuracy [11]. In the engineering field, severe errors may be caused due to the electrochemical erosion effect and polarization effect of the electrodes after long-time contact with the conductive liquids [8]. Besides, the contamination of the electrodes would bring measurement deviations [12]. In 2010, a contactless approach termed capacitively coupled electrical resistance tomography (CCERT) was proposed by Wang et al. [12-14]. Based on the capacitively coupled contactless conductivity detection (C^4D) technique, CCERT avoids contact error by inserting an insulation layer between the electrodes and conductive contents [11]. Besides, experiments show that CCERT could have a larger excitation frequency domain than that of traditional ERT, which results in better imaging results [15,16]. Therefore, CCERT is attracting more and more researchers' attention. So far, CCERT has been applied in gas-liquid two-phase materials, brain imaging, breast cancer detection, etc. [16-18].

Like other electrical tomography (ET), CCERT also has the highly nonlinear and ill-posed inverse problem. Traditional algorithms used to solve the ET inverse problem include non-iterative methods and iterative methods, facing the challenges of reconstruction speed and accuracy [19]. In the last several years, with the development of GPU, deep learning (DL) algorithm has shown its promising potential in image application and has also been suggested as an alternative for inverse problem solving. Inspired by the neuronal network of the human brain, DL adopts machine learning algorithms to model sophisticated abstractions of the raw input data through a deep architecture containing multiple hidden layers to implement linear and non-linear transformations [20]. Although the history of DL dates back to 1965, it has only been rapidly developed in recent years, mainly in the improved computational abilities and nonlinearities solving abilities, and these fast improvements therefore increase the network depth [21,22]. Up to now, Deep neural network (DNN) has been applied to solve the inverse problem of imaging, super-resolution, de-noising, film colourisation, etc. [23,24]. Since DNN is flexible on high-dimensional function expression, it can theoretically approximate the entire inverse map, thus avoiding the iterative process [25]. More studies on DNNs in inverse problems solving can be found in [26,27].

For ET techniques, DNN algorithms are also suggested as a way to solve the inverse problem and reconstruct images. Convolutional neural network (CNN), one of the most often-used DNN model, has the properties of deep, fully connected, and feedforward. As CNN is good at extracting essential features from the input data and mapping nonlinear functions, it is relatively computational efficient compared to other DNN method [28]. In the recent studies, the cascaded end-to-end convolutional neural network (CEE-CNN) was built by Wei et al. to apply the induced-current learning method (ICLM) to solve the nonlinear reconstruction problem in EIT [29]; motivated by the linear perturbation analysis of the forward map, Fan et al. used the BCR-Net based neural network to approximate both the forward and inverse maps, using the proposed neural network to replace the traditional Dirichlet-to-Neumann (DtN) map [25]. More studies of CNN based ET applications can be viewed in [30,31]. In addition, the studies of Artificial Neural Network (ANN), another popular DNN model, have also attract lots of interests for ET application. Fernández-Fuentes et al. developed an ANN-based inverse problem solver for EIT, which takes the boundary measurements as input and generates the conductivity value of each mesh triangular elements of the image [32]. Rymarczyk et al. compared some machine learning algorithms for industrial ET, including ANN, LARS and Elastic net methods, and

they used a set of trained subsystems to generate the value of each pixel of image in parallel [33].

In this work, a multi-layer feedforward CNN was established to achieve the image reconstruction for CCERT industrial application. During the training, the 2D monochrome 2500-pixel image was divided into 625 clusters, then the proposed CNN was trained separately for each pixel cluster of the image to achieve the feature extraction and classification. Supervised learning algorithm built a mathematical model for the cluster to map the input resistance to the output pixel pattern. With the 12-electrode circular CCERT system, the proposed multiple-layer CNN model was examined by both simulation and experiment data. In addition, the reconstructing images obtained with the CNN method were compared with the images produced by a traditional reconstruction algorithm, TV algorithm.

2. Methods

2.1. System configuration and data acquisition principle

For CCERT system, data is collected via the boundary-placed electrodes, this research studied the performance of a circular-electrode sensor where 12 electrodes are evenly spaced and attached to the outside of the sensing area with an angel of 25°, as shown in Figure 1a. The size of one electrode is 150 mm*24 mm, the inner and outer diameter of the sensing area is 106 mm and 110 mm, respectively.

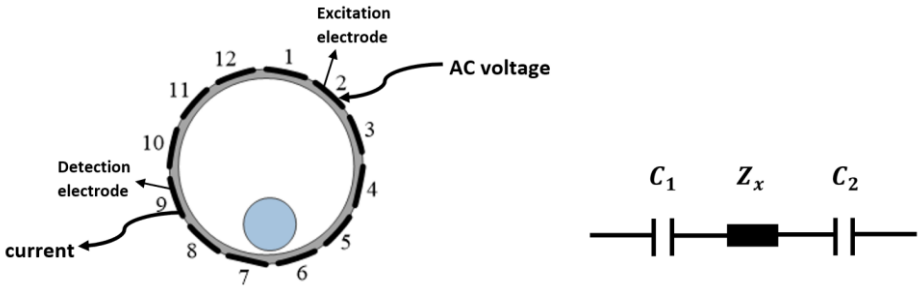

Figure 1. (a) Demonstration of an electrode-pair. (b) Equivalent detection circuit.

During the measurement process, the 3.3V AC voltage with 500 kHz was applied as the excitation signal. For each independent measurement, only two electrodes are selected as the exciting and detecting electrode pair, where the AC voltage is injected to the excitation electrode and the current is detected via the detection electrode, and the remaining electrodes are kept at floating potentials at the same time. The equivalent detection circuit can be simplified as Figure 1b, in which C_1 and C_2 express the coupling capacitances, Z_x represents the impedance of the sensing area. Only the resistance part is involved in the CCERT system, and it can be calculated from the applied voltage and the real part of the detected current based on the Ohm' Law. In a complete measurement cycle, electrode 1 is firstly selected as the excitation electrode, and electrode 2 to electrode 12 is successively selected as the detection electrode. Following this step, electrode 2 is selected as the excitation electrode, and the remaining electrodes are selected as the detection electrode in turn. The whole process continues until electrode 11 and 12 constitute an electrode-pair. For the same sample, detected resistance between a certain electrode-pair keeps the same no matter which acts as the excitation electrode and the detection electrode. Therefore, in each measurement cycle, the total number of independent measurements is: $\frac{n(n-1)}{2} = \frac{12*(12-1)}{2} = 66$, where n is the number of electrodes.

2.2. Conventional forward modeling and image reconstruction algorithm of CCERT

The conventional CCERT is the technique that enables to reconstruct the internal conductivity distribution from the boundary resistance measurements with the sensitivity matrix and reconstruction algorithm. The imaging process has two essential stages, one is the forward modelling, and the other is image reconstruction, often termed as the inverse problem [34]. During the test, time-difference (TD) method is adopted to obtain the resistance projection (P), where P equals to the subtraction of resistances at different times: one with homogeneous conductive background and the other with detected samples added into the background [35]. Tap water with a conductivity of σ=0.018 S/m was taken as the background medium.

In forward problem, boundary equations are obtained based on the known conductivity distribution within the target region. Two assumptions are made in the forward modelling process. The first assumption is that the electromagnetic field can be regarded as a quasi-static electric field, since the detected area is much smaller than the wavelength of the excitation signal under the commonly applied frequencies [18]. The second one is that the fringe effect caused by the finite electrode length can be neglected in order to simplify the modelling process [18]. Therefore, based on Maxwell's equations, the forward problem at the under-radio frequency within the sensing area Ω can be written as [11]:

$$\nabla \cdot \left(\left(\sigma(x,y) + j\omega\varepsilon(x,y)\right)\nabla u(x,y)\right) = 0,\ (x,y) \subseteq \Omega \tag{1}$$

where $\sigma(x,y)$, $\varepsilon(x,y)$ and $u(x,y)$ are the conductivity, permittivity, and electrical potential distribution of the sensing area. ω is the angular frequency of the excitation signal, ($\omega = 2\pi f$, f is the excitation frequency). ∇ represents the gradient operator. Then, the boundary conditions can be derived as:

$$\begin{cases} u_a(x,y) = V & (x,y) \subseteq \Gamma_a \\ u_b(x,y) = 0 & (x,y) \subseteq \Gamma_b \\ \frac{\partial u_c(x,y)}{\partial \vec{n}} = 0 & (x,y) \subseteq \Gamma_{c\ (c \neq a,b.)} \end{cases} \tag{2}$$

where V is the amplitude of the excitation voltage, $\vec{n}$ represents the normal unit vector pointing out of the boundary. a, b, and c are the indexes of the excitation electrode, the detection electrode, and the remaining floating electrodes, respectively. Γ_a, Γ_b and Γ_c are the spatial locations of the corresponding electrodes.

Then, the sensitivity matrix (S), which reveals the relationship between the resistance projection (P) and conductivity distribution (G) can be determined based on the simulation [12]. During the forward simulation, a critical process is to mesh the sensing region and the system model into a finite number of elements. In this work, the discretization process is conducted by COMSOL Multiphysics. The simulation process is carried out by MATLAB as well as COMSOL Multiphysics. The excitation AC voltage is simulated as a 500 kHz frequency and 1V amplitude signal. After injecting the AC voltage signal to the electrode, the i^{th} current measurement on the detection electrode can be represented as:

$$I_i = \int J_{m-n}\, d\Gamma \tag{3}$$

where I_i is the i^{th} current measurement ($i = 1,2,\ldots,66$), J_{m-n} is the measured current density of the electrode pair m and n. Then the corresponding i^{th} resistance measurement between the electrode pair can be written as:

$$R_i = Real\left(\frac{V_i}{I_i}\right) = Real\left(\frac{1}{I_i}\right) \tag{4}$$

With the whole measurement data, the sensitivity matrix of CCERT is:

$$S = \begin{bmatrix} S_{11} & \cdots & S_{1N} \\ \vdots & \ddots & \vdots \\ S_{M1} & \cdots & S_{MN} \end{bmatrix} \tag{5}$$

$$S_{ij} = \frac{\partial I}{\partial \sigma} = \frac{Real(I_i^j - I_i^0)}{\sigma_1 - \sigma_0} = \frac{1/R_i^j - 1/R_i^0}{\sigma_1 - \sigma_0}, \qquad (S_{\mathrm{ij}} \subseteq S) \tag{6}$$

where M is the total number of measurements, N is the total number of meshing elements. S_{ij} is the sensitivity matrix associated with the i^{th} measurement and j^{th} element. I_i^0 and R_i^0 are the i^{th} current and resistance measurement when the imaging region is at background state, where the conductivity of all elements equals to σ_0. When the conductivity of j^{th} element changes from σ_0 to σ_1 while the remaining elements still have σ_0 conductivity , the i^{th} current and resistance measurement then becomes I_i^j and R_i^j.

After calculating the sensitivity matrix, the image reconstruction process can be conducted. For simplicity, the approximated linear relationship between P (change in resistance measured data), S and G (change in electrical conductivity) can be expressed as:

$$P = SG \tag{7}$$

The inverse problem cannot be solved directly by multiplying P and the inverse of S to obtain G, given the following reasons. Firstly, the solution is under-determined since there are more variables than equations [11]. Secondly, G is very sensitive to the perturbations of P [11]. Additionally, CCERT is a soft-field tomography, which means the actual sensitivity matrix changes with the conductivity distribution [11]. So proper image reconstruction algorithms are needed in order to solve the inverse reconstruction problem.

For circular CCERT, linear back projection (LBP) was adopted firstly due to its advantages of simplicity and rapidity, but the image quality was limited. So, an algorithm which combined LBP with a K-means clustering method was proposed to improve the image quality [36]. In 2014, a new hybrid algorithm which adopted Tikhonov regularisation as the initial guess and took the simultaneous iterative reconstruction technique (SIRT) for standard iterations was proposed [12]. In 2017, the method which is the combination of the Levenberg-Marquardt (L-M) method and the simultaneous algebraic reconstruction technique (SART) was put forward, this method applied L-M for initial guess and SART for final reconstruction [37]. Recently, the total variation (TV) algorithm with split Bregman iterations was used for CCERT reconstruction [15].

A simple image reconstruction can be done using LBP:

$$G \approx S^T P \tag{8}$$

An iterative TV algorithm is an effective method for recovering and reconstructing piecewise-constant signals, while it is a deterministic technique that safeguards discontinuities in image processing tasks, so it is well suited for this two-phase imaging.

An anisotropic TV regularization term is expressed by (9):

$$R_{ITV}(G) = \sum_j \left|\left|D_j \, \mathrm{G}\right|\right|_1 \tag{9}$$

where D_j represents a finite-difference approximation of the spatial image gradient. An isotropic version of the TV function is given by Equation (10) and was used in this work.

$$G = arg\,min_{\,G} \left(\alpha \left|\left|\nabla G\right|\right|_1 \right), \; s.t. \left|\left|SG - P\right|\right|^2 < q \tag{10}$$

q is the error threshold. α is the regularization parameter. The higher the regularization (smoothing) parameter gets, the more impact the regularization will have on the solutions, and consequently, the more details will be lost from the image. Indeed, with the increase of α, the contrast of the image becomes lower, and the boundaries within the object become smoother. After carefully choosing the regularization parameter, we optimized the image by deleting the artefacts. A more detailed description of the proposed TV method for CCERT can be seen in [15]. To be able to compare with the binary CNN algorithm, the TV reconstructed images are the thresholds for the binary images.

2.3. CNN-based Image reconstruction CCERT

The supervised learning algorithm is one kind of machine learning algorithms. As task-driven learning, it aims to find a mathematical model of mapping the inputs and their correct outputs through back propagation (BP) learning algorithm. It is commonly applied for various classification problems including image classification, fraud detection and

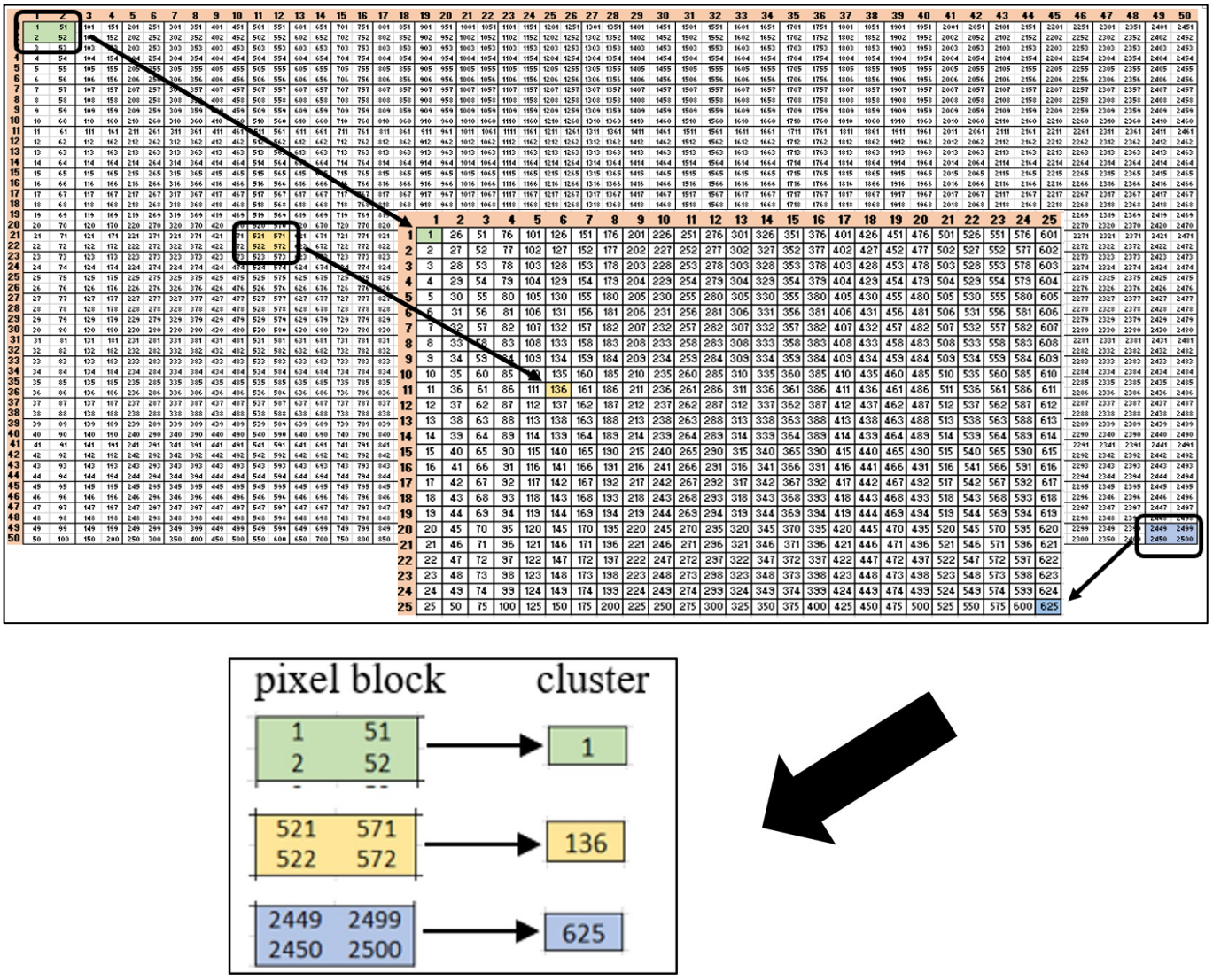

Figure 2. Conversion between pixels and clusters: the whole picture of the pixels and the demonstration of conversion process.

diagnostics as well as regression problems including risk assessments, score prediction and market forecasting.

In this research, a CNN-based supervised learning algorithm was adopted for image reconstruction, which established a mathematical model of mapping the input 66 resistance measurements to the desired output pixel pattern [38]. The result image is meshed into grid with 50-by-50 pixel, and the pixels are equally spaced. These 2500 pixels are sorted first by row and then by column. So, in the first column, from the first row to the last row, the pixels are numbered from 1 to 50. Then, in the second column, from the first row to the last row, the pixels are numbered from 51 to 100. Following the same rule, the pixels in the last column from the first row to the last row is numbered from 2451 to 2500. If a single CNN were used to image the entire 2500-pixels image, there would be 2^{2500} pixel distribution classes for CNN to classify, which would be almost impossible for training. The problem was solved by dividing the 50-by-50-pixel image into 25-by-25 non-overlapping clusters, with each cluster representing a 2-by-2-pixel block. Since the space of each pixel point on the image is same, the space of cluster is also the same among each other. The conversions between pixels and clusters can be viewed in Figure 2. The clusters are also sorted first by row then by column. Thus, take cluster 1 as an example, it corresponds to the area of pixel 1, 2, 51 and 52.

Table 1. Pixel distributions within one cluster.

Label Number	1	2	3	4	5	6	7	8	9	10	11	12	13	14	15	16
Binary Matrix	1 1 1 1	1 1 0 1	1 0 1 1	0 1 1 1	1 1 1 0	1 0 0 1	0 1 1 0	0 0 1 1	1 1 0 0	1 0 1 0	0 1 0 1	0 0 0 1	1 0 0 0	0 0 1 0	0 1 0 0	0 0 0 0
Pixel Pattern																

After completing the transformation, distinct CNN could be applied for each cluster, and the classification became feasible since there are $2^4 = 16$ pixel patterns within one cluster, their labelling and matrix expressions are displayed in Table 1. As the proposed CNN model is designed for the two-phase material application, the result can be represented as the binary image, where 0 and 1 mean the background and inclusion.

Then, the image reconstruction can be realized by the conversion process via the 625 CNN models as shown in Figure 3. The 625 CNN results are converted into 625 2-by-2 binary matrices based on Table 1, and the conversion between cluster patterns and the final pixel image takes the reverse of the conversion from pixel to cluster as explained in Figure 2, to form the final 50-by-50-pixel image. The development of each CNN followed the general procedure of deep learning method as shown in Figure 4, which mainly includes accessing data, constructing network architecture, setting training options, and conducting training, along with hand-tunings to achieve a fitting model.

Simulation data were generated based on the pre-calculated sensitivity matrix (S) and was labelled for each CNN based on the cluster's pixel pattern. 10000 cases were generated for the network training, containing 5000 single-inclusion cases, 2500 double-inclusion cases, and 2500 triple-inclusion cases. All the inclusions are in the quasi-circular shape of diameter from 10 pixel-length to 20 pixel-length placed on all locations of the image. Random noise was added to the simulation based on the standard deviation value of the background measurement for network training. Each set of 66 resistances were scaled to [0 1] to avoid gradient vanishing and converted into an 11-by-6 matrix. The structure of the matrix can be any combinations of size 66, such as 11-by-6, 6-by-11, or 2-by-33. The final result will be the same no matter what matrix structure is used.

The CNN layers were constructed with the aid of deep network designer app of MATLAB. After hand-tunings, the 625 CNNs adopted the same 19-layer architecture to

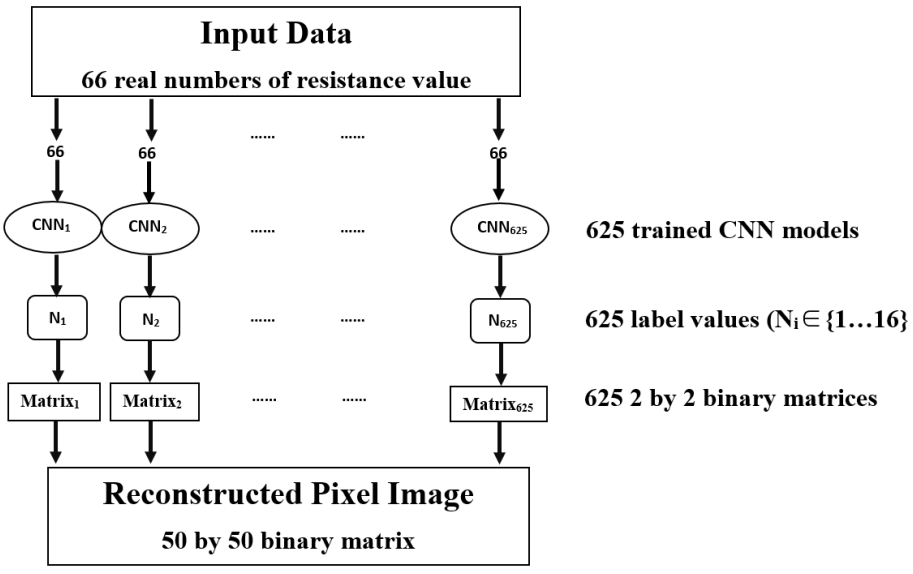

Figure 3. The reconstruction processes.

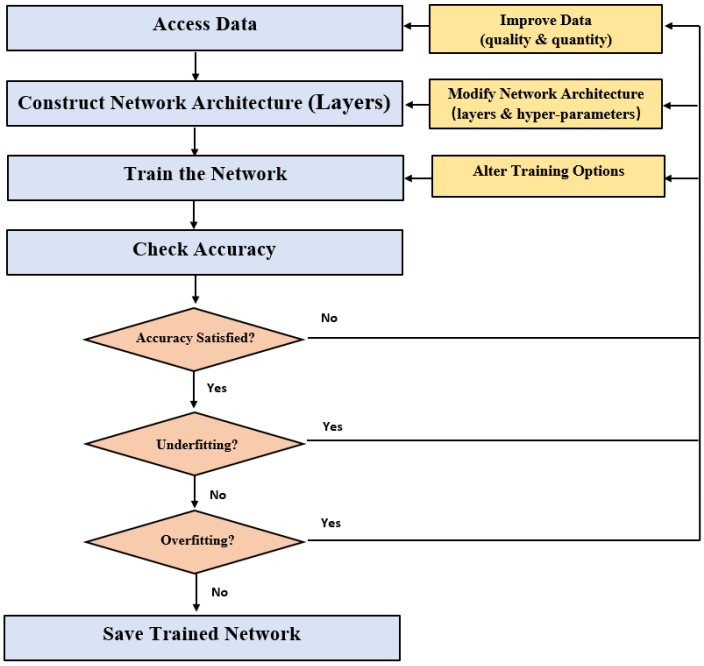

Figure 4. The CNN model development.

realize feature extraction and classification, the network architecture is displayed in Figure 5. In this work, hand-tuning of hyperparameters includes: (1) tuning hyperparameters related to the network structure, such as the number of hidden layers and units, the activation function, etc. (2) tuning hyperparameters related to the training algorithm, such as optimizer, initial learning rate, number of epochs, batch size, etc. For different cases, the hand-tuning is different, but the trade-off needs to be considered along the training to avoid underfitting or overfitting cases. Convolution layers function as feature extractors by executing convolution operations between the receptive fields of the input and the kernels. Activation function, rectified linear unit (ReLU), introduces nonlinearity to the network via $ReLU(x) = \max(x, 0)$. Max pooling does non-linear down-sampling on each feature map by taking the max value of the feature block to reduce computation while keeping essential information and providing invariance to local translation. Batch normalisation improves the stability, performance, and the speed of the network. Fully connected (FC) layer flattens the 3D features into a 1D vector for classification, and softmax layer calculates the probability of the input data belonging to each class. The distribution of 16

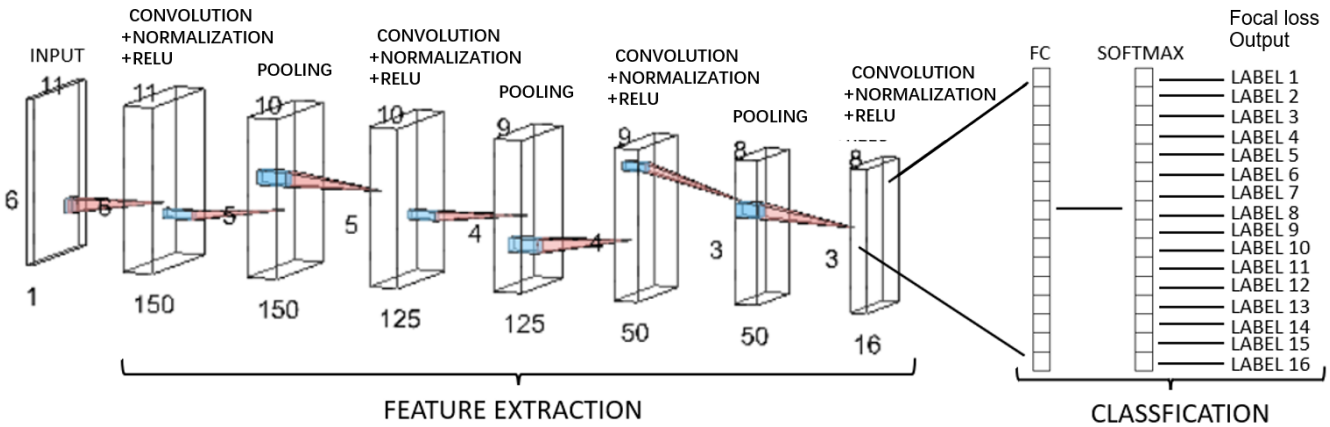

Figure 5. The CNN architecture illustration.

pattern classes is unbalanced. After randomly sampling the different cases, Table 2 shows the 16 classes distribution for all sampled cases. Though the appearing number of each classes may vary with the added noise, class 1 and class 16 account for the majority of possibilities. Thus, the focal loss layer is critical since it is applied as the output layer to deal with the data imbalance between classes. The details of CNN layers and parameters are given in Table 3.

Table 2. 16 classes distributions of sampled cases. (Each case has 625 distribution possibilities)

CASE / CLASS	With a single 14-pixel length inclusion	With a single 16-pixel length inclusion	With 14- and 16-pixel length inclusions	With 16-, 14-, and 12-pixel length inclusions
1	45	34	82	102
2	0	1	0	3
3	0	1	0	3
4	0	1	0	3
5	0	1	0	3
6	0	0	0	0
7	0	0	0	0
8	3	3	5	3
9	3	3	5	3
10	3	0	5	3
11	3	0	5	3
12	1	1	1	4
13	1	1	1	4
14	1	1	1	4
15	1	1	1	4
16	564	577	519	483

Table 3. Details of CNN layers and parameters.

Layer	Name and Type	Operation	Activations	Learnable
1	Imageinput (Image input)	$11 \times 6 \times 1$ images with 'zerocenter' normalization	$11 \times 6 \times 1$	-
2	conv_1 (Convolution)	150 $3 \times 3 \times 1$ convolutions with stride [1 1] and padding 'same'	$11 \times 6 \times 150$	Weights $3 \times 3 \times 1 \times 150$ Bias $1 \times 1 \times 150$
3	batchnorm_1 (Batch Normalization)	Batch Normalization with 150 channels	$11 \times 6 \times 150$	Offset $1 \times 1 \times 150$ Scale $1 \times 1 \times 150$
4	relu_1 (ReLU)	Relu	$11 \times 6 \times 150$	-
5	maxpool_1 (Max Pooling)	2×2 max pooling with stride [1 1] and padding [0 0 0 0]	$10 \times 5 \times 150$	-
6	conv_2 (Convolution)	125 $3 \times 3 \times 150$ convolutions with stride [1 1] and padding 'same'	$10 \times 5 \times 125$	Weights $3 \times 3 \times 150 \times 125$ Bias $1 \times 1 \times 125$
7	batchnorm_2 (Batch Normalization)	Batch Normalization with 125 channels	$10 \times 5 \times 125$	Offset $1 \times 1 \times 125$ Scale $1 \times 1 \times 125$
8	relu_2 (ReLU)	Relu	$10 \times 5 \times 125$	-

9	maxpool_2 (Max Pooling)	2×2 max pooling with stride [1 1] and padding [0 0 0 0]	$9 \times 4 \times 125$	-
10	conv_3 (Convolution)	50 $3 \times 3 \times 125$ convolutions with stride [1 1] and padding 'same'	$9 \times 4 \times 50$	Weights $3 \times 3 \times 125 \times 50$ Bias $1 \times 1 \times 50$
11	batchnorm_3 (Batch Normalization)	Batch Normalization with 50 channels	$9 \times 4 \times 50$	Offset $1 \times 1 \times 50$ Scale $1 \times 1 \times 50$
12	relu_3 (ReLU)	Relu	$9 \times 4 \times 50$	-
13	maxpool_3 (Max Pooling)	2×2 max pooling with stride [1 1] and padding [0 0 0 0]	$8 \times 3 \times 50$	-
14	conv_4 (Convolution)	16 $3 \times 3 \times 50$ convolutions with stride [1 1] and padding 'same'	$8 \times 3 \times 16$	Weights $3 \times 3 \times 50 \times 16$ Bias $1 \times 1 \times 16$
15	batchnorm_4 (Batch Normalization)	Batch Normalization with 16 channels	$8 \times 3 \times 16$	Offset $1 \times 1 \times 16$ Scale $1 \times 1 \times 16$
16	relu_4 (ReLU)	Relu	$8 \times 3 \times 16$	-
17	fc (Fully Connected)	16 fully connected layer	$1 \times 1 \times 16$	Weights 16× 384 Bias 16×1
18	softmax (Softmax)	Softmax	$1 \times 1 \times 16$	-
19	focallossoutput (Focal Loss Layer)	Focal Loss Layer	-	-

The training was carried out on each CNN separately through the BP algorithm and Adam optimizer, in order to find the most suitable weights and bias for the model which could result in minimal prediction cross-entropy loss. The simulation dataset was divided into training data, validation data and test data as the ratio of 80%: 10%: 10% randomly. The 'initial learning rate' was set as 1e-5, 'MaxEpochs' was 20, 'MiniBatchSize' was 50, the validation frequency was 20, and the rest configuration parameters were set as default. The optimization process went through maximumly 3380 iterations before reaching the final convergence. For these 625 CNN networks, the minimum validation accuracy after training is 85.6% and the average validation accuracy is 94.4%. The number of clusters with the validation accuracy above 90% is 536, accounting for 85.7% of all clusters. Figure 6 displays the training-progress plot generated by MATLAB for the 313^{rd} cluster, which is the hardest one to reconstruct as it is located in the center of the sensing area. Due to the characteristic of the soft-field, the sensitivity in the center area is lower than that near to the sensor. In Figure 7b, the validation and test accuracy of the other clusters are also shown. The selected demonstrating clusters are positioned at the midline of the vertical axis with the same space. Figure 7a shows the position of the selected cluster with red squares, and the corresponding clusters are the 63^{rd}, 188^{th}, $313^{rd,}$ 438^{th}, 563^{rd} cluster. From the result, it can be known that the cluster near the sensor area will have a better CNN performance. In Figure 6, the deep blue curve and black curve in the top image represent the training accuracy and validation accuracy, the orange curve and black curve in the bottom image represent the training loss and validation loss. With the growing training iterations, the accuracy curves increased gradually, achieving over 85.6% after training, while the loss curves decreased. Based on the tendency of the curves, it can be regarded as a good fit network. Besides, the accuracy on test dataset for the 313^{rd} cluster reached 85.93%, verifying the generalization ability of the model.

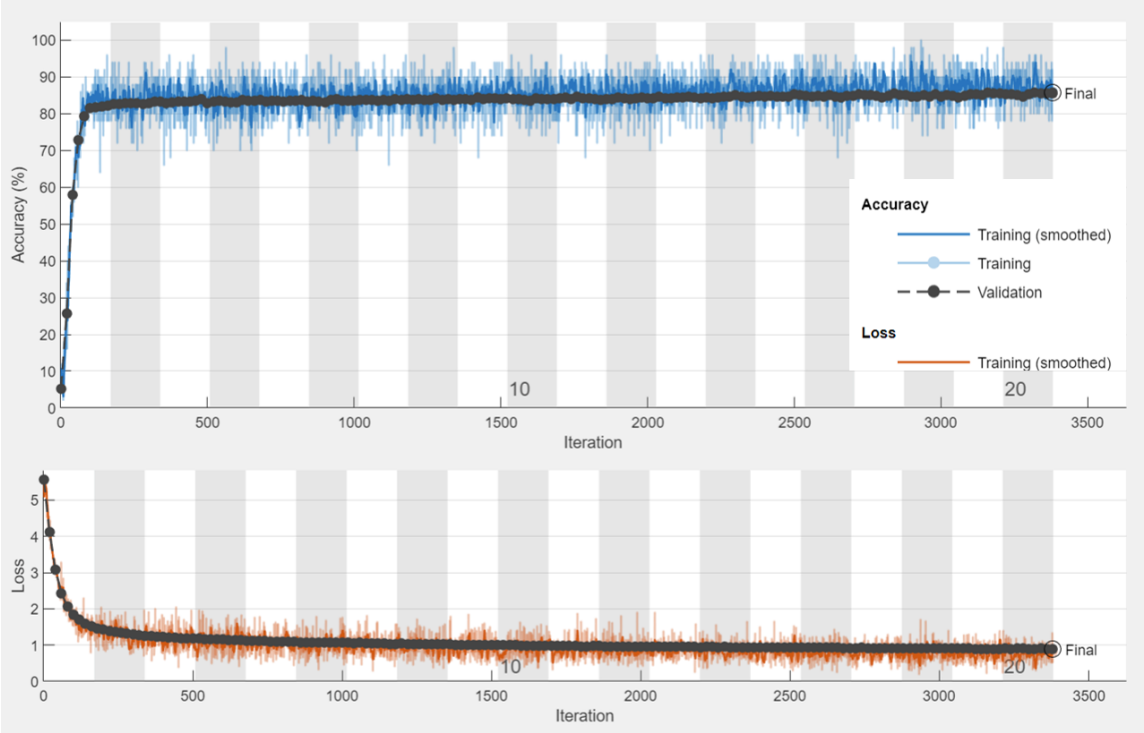

Figure 6. The training-progress plot for cluster 313^{rd} generated by MATLAB

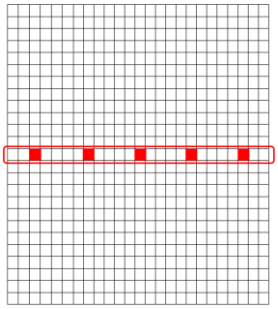

(a)

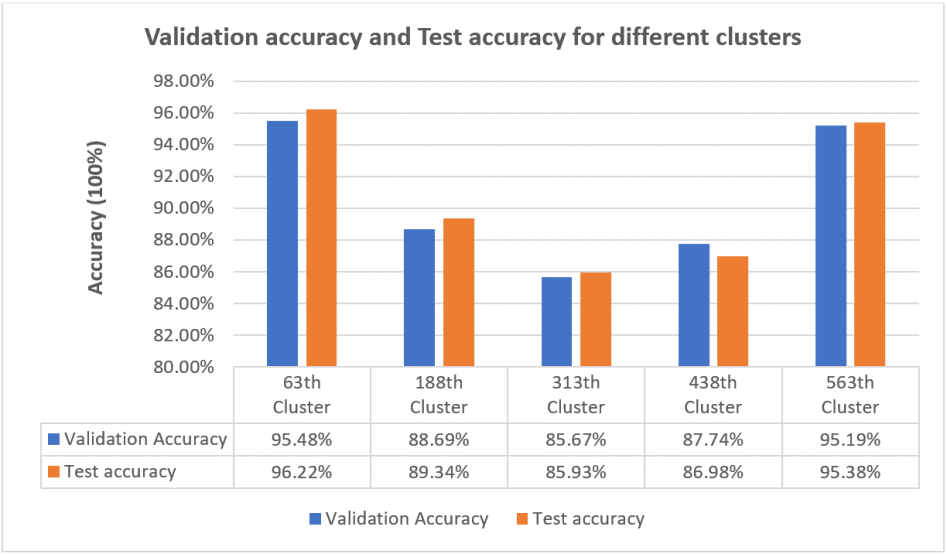

(b)

Figure 7. (a) The cluster grid and the selected clusters (marked with red squares) for training accuracy comparison (Training accuracy for clusters positioned at difference place.)

When assess the performance of CNN, if the dataset used to the train the network is unbalanced, the trained network may be underfitted. So, metrics other than accuracy are needed to assist in the analysis, such as the Confusion matrix (including Recall and Precision value), and the ROC curve. In our design, since we trained the distinct CNN for each cluster instead of individual pixels, and these 16 classes of the same cluster will not have the same occurring probability, thus, there are variabilities in the recall and precision values of different classes for the same cluster. Classes 1 and 16 have the highest occurring probability, therefore, the precision and recall values of 625 CNNs for these two classes

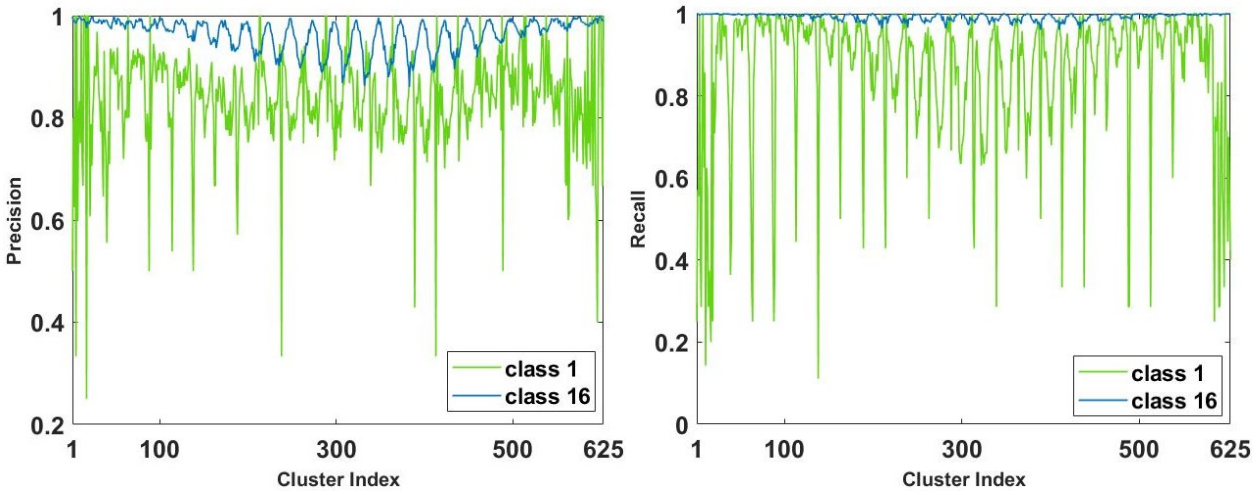

(a) (b)

Figure 8: The plot of (a) precision and (b) recall values of 625 CNN networks for class 1 and class 16.

are relatively stable and high, and the metrics show the characterstics that the value is smaller when the cluster is at the center area while larger when the cluster is close to the sensor. Figure 8 shows the plot of precision and recall values of 625 CNN networks for class 1 and class 16. For class 16, the minimum precision and recall value of the 625 CNNs is 86% and 96%, respectively. For class 1, though a few networks underperformed, in aggregate 85.9% of networks achieved more than 75% precision value and 79.6% of networks achieved more than 75% recall value. For the other classes, the performance of network varied among clusters, and the values of these metrics are low, mostly below 20%. Although such results may introduce errors in boundary reconstruction, it is necessary to train the network with all 16 classes. By training the network with more different cases, the performance of 625 CNNs for classfication can be improved, thus providing the images with more accurate boundaries.

Compared to other simple networks such as the Shallow Neural Network, our proposed 625 multi-layer deep neural network performs better. 625 CNNs possess an average accuracy of 94.4%, and have high precision and recall values for class1 and class16, which are the most important two classes. Take the 63rd, 188th, 313rd ccluster as examples, the test accuracy of 625 CNN is 96.22%, 89.34%, and 85.93%, while the accuracy of Shallow network with the same 150 depth is 93.7%, 84%, and 83.7%, respectively. Moreover, the recall and precision values of 625CNN for class 1 and class 16 are much higher than those of the shallow network, implying that the shallow network has a higher probability of misclassifying class 1 or class 16 as other classes, which will affect the image results. Judging from the complete simulation and experimental image result shown in the following sections, our network is able to correctly determine the location and size of the inclusions, and the performance of the system meets our design goals.

The 625 CNN models were saved separately and applied for simulation reconstruction and experimental reconstruction. The image reconstruction accuracy is analyzed quantitatively by calculating the structural similarity (SSIM), the mean squared error (MSE), and the peak signal-to-noise ratio (PSNR) between the reconstructed image and the referencing image. SSIM, MSE, and PSNR are all metrics used to assess the image quality [39,40]. MSE is the average energy of the difference between the current image and the referencing image, PSNR is the ratio between the energy of the peak image value to the mean energy of the noise. The calculations of these two methods are both based on the error between the corresponding pixel points. Suppose there are two images, the current image X and the referencing image Y. The total number of pixels is N for both images,

and the pixel value belonging to them is x_i and y_i respectively. Then, the calculating algorithm of MSE and PSNR can be expressed as:

$$MSE = \frac{1}{N}\sum_i^N (e_i)^2 = \frac{1}{N}\sum_i^N (x_i - y_i)^2 \quad (11)$$

$$PSNR(in\ dB) = 10 \cdot \log_{10}\frac{L^2}{MSE} = 20 \cdot \log_{10}\frac{L}{\sqrt{MSE}} \quad (12)$$

where L is the maximum pixel value of the current image. The less distorted image should have a higher PSNR value but a lower MSE value.

SSIM is an index showing the similarity between two images. Different from MSE and PSNR, SSIM evaluates the quality of an image with a region of pixels instead of the individual pixel points, thus it conforms the human visual system. It calculates the similarity between the images in terms of luminance, contrast, and structure. The formulation of SSIM is:

$$SSIM = \frac{(2\mu_x\mu_y + c_1)(2\sigma_{xy} + c_2)}{(\mu_x{}^2 + \mu_y{}^2 + c_1)(\sigma_x{}^2 + \sigma_y{}^2 + c_2)} \quad (13)$$

where μ_x is the average of x, μ_y is the average of y; $\sigma_x{}^2$ and $\sigma_y{}^2$ are the variance of x and y; σ_{xy} is the covariance of x and y; c_1 and c_2 are the variables that stabilize the division. The value range of SSIM is among 0-1, and the image with a better quality should have a higher SSIM value.

3. Results

3.1. Simulation reconstruction results

In all simulation and experiment results, binary images are used, and they were cut into circular shape to match the shape of the sensing system. Reconstruction results obtained via traditional TV algorithm are also given. For accuracy analyses of TV result and CNN result, we used the input simulation image as the reference ('True' image). To give a better comparison between two methods, the term 'TV-CNN' is also given. It takes the TV result as the reference, and thus shows the difference between the CNN results and reference.

Table 4 gives the results of 9 simulation cases, in which cases No.1-3 and cases No.4-6 contain single inclusion with the diameter of 16-pixel length and 14-pixel length respectively, cases No.7-8 are for double inclusions with diameters of 16-pixel and 14-pixel length, case No.9 includes three inclusions with diameters of 16-pixel, 14-pixel and 12-pixel length. For a better comparison, the initial pixel images recovered by CNN were converted from binary image to RGB image with our MATLAB drawing function. Since during the training process, some noise was added to the simulated measured data, so the noise in data translates to artifacts in image domain. In real experiments, we have the true 0 and 1 situation representing the conducting and nonconducting materials, any value in between is ignored.

Table 4. Details Simulation reconstruction results and accuracy analyses.

Case	Image Reconstruction Illustrations	Evaluation Metrics		
1	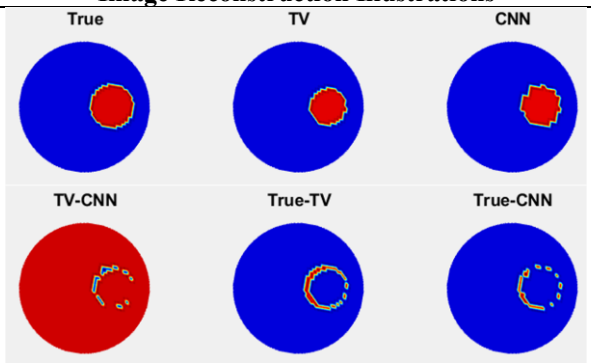	SSIM	CNN	0.9011
			TV	0.8544
			TV-CNN	0.9215
		MSE	CNN	0.0140
			TV	0.0240
			TV-CNN	0.0100
		PSNR	CNN	18.5387
			TV	16.1979
			TV-CNN	20.0000

2	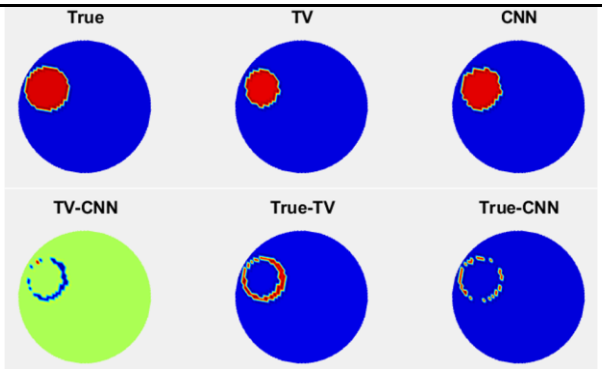	SSIM	CNN	0.9150
			TV	0.8425
			TV-CNN	0.8863
		MSE	CNN	0.0124
			TV	0.0296
			TV-CNN	0.0180
		PSNR	CNN	19.0658
			TV	15.2871
			TV-CNN	17.4473
3	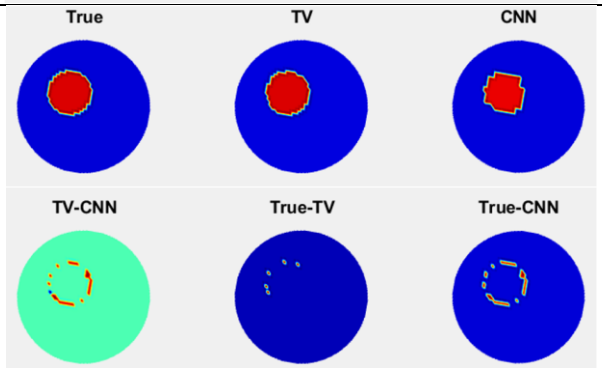	SSIM	CNN	0.9043
			TV	0.9842
			TV-CNN	0.9131
		MSE	CNN	0.0132
			TV	0.0020
			TV-CNN	0.0120
		PSNR	CNN	18.7943
			TV	26.9897
			TV-CNN	19.2082
4	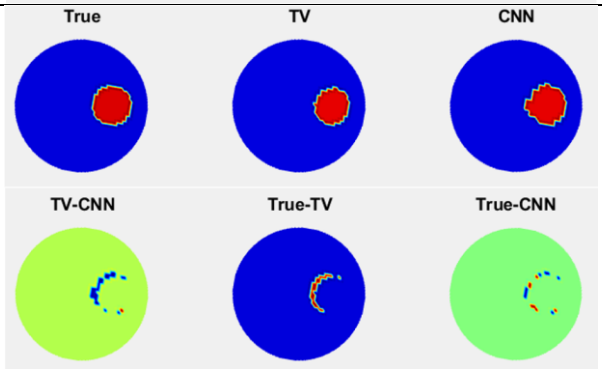	SSIM	CNN	0.9502
			TV	0.9270
			TV-CNN	0.9170
		MSE	CNN	0.0064
			TV	0.0116
			TV-CNN	0.0132
		PSNR	CNN	21.9382
			TV	19.3554
			TV-CNN	18.7943
5	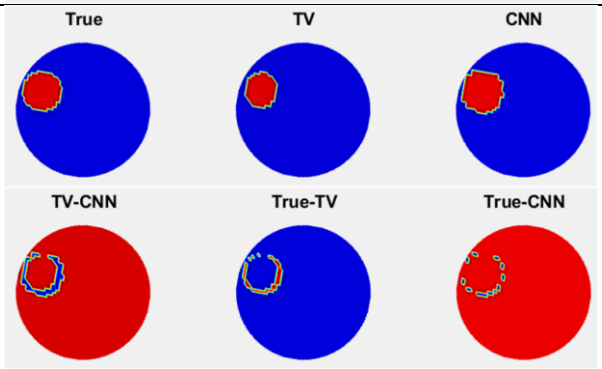	SSIM	CNN	0.9288
			TV	0.8886
			TV-CNN	0.8576
		MSE	CNN	0.0092
			TV	0.0184
			TV-CNN	0.0276
		PSNR	CNN	20.3621
			TV	17.3518
			TV-CNN	15.5909
6	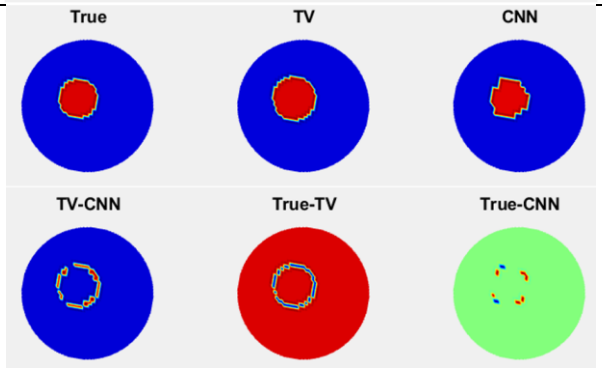	SSIM	CNN	0.9538
			TV	0.8735
			TV-CNN	0.8668
		MSE	CNN	0.0060
			TV	0.0168
			TV-CNN	0.0196
		PSNR	CNN	22.2185
			TV	17.7469
			TV-CNN	17.0774

7	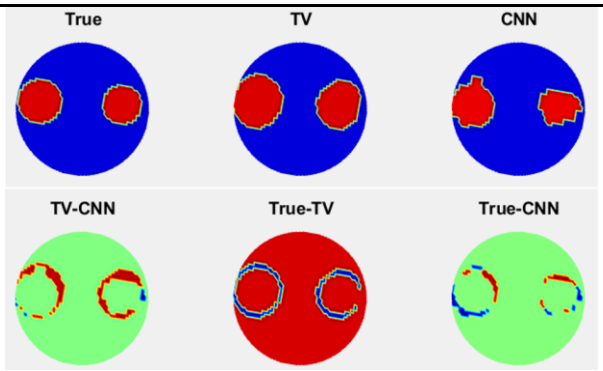	SSIM	CNN	0.7713
			TV	0.6736
			TV-CNN	0.6740
		MSE	CNN	0.0388
			TV	0.0568
			TV-CNN	0.0660
		PSNR	CNN	14.1117
			TV	12.4565
			TV-CNN	11.8046
8	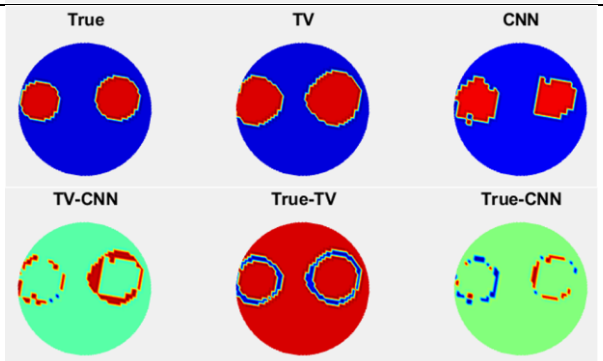	SSIM	CNN	0.7660
			TV	0.6240
			TV-CNN	0.6574
		MSE	CNN	0.0356
			TV	0.0704
			TV-CNN	0.0724
		PSNR	CNN	14.4855
			TV	11.5243
			TV-CNN	11.4026
9	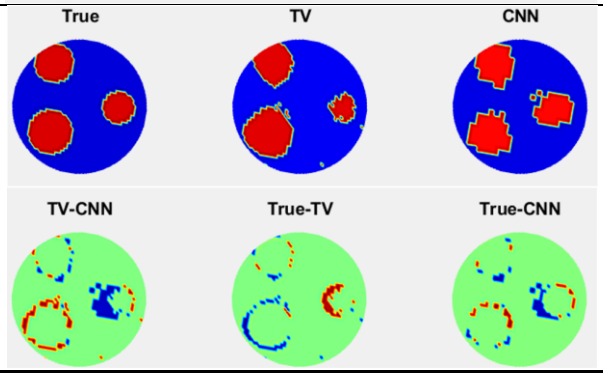	SSIM	CNN	0.7016
			TV	0.5970
			TV-CNN	0.4947
		MSE	CNN	0.0472
			TV	0.0604
			TV-CNN	0.0868
		PSNR	CNN	13.2606
			TV	12.1896
			TV-CNN	10.6148

From the above table, we can see that the 625 CNN models can effectively reveal the number, size, and position of the simulated inclusions, with the average SSIM of 0.8658, average MSE of 0.0203, and average PSNR of 18.0856. With the increasing number of inclusions, the SSIM drops and MSE increases, while still, it can reach the SSIM of over 0.7 and MSE of less than 0.05 for three-samples detection. The consistency between the TV results and CNN results verifies the reliability of the CNN models and provides feasibility for experimental reconstruction.

3.2. Experimental reconstruction result

Experimental data was collected from the CCERT system as shown in Figure 9a and 9b, which includes an insulating pipe, a 12-electrode circular array sensor, 12 excitation and detection units, a signal control and processing unit and a micro-computer. Plastic rods with diameters of 34.5mm, 29.5mm and 26.5mm were utilized as detected samples, which approximately matched the simulated inclusions with diameters of 16-pixel, 14-pixel, and 12-pixel respectively. Their distributions also corresponded to the examined simulation cases in Table 4, so that we took the same simulation image as the true image for each case. TD method was adopted to eliminate background effects. Same as the simulated training data, each set of 66 experimental resistances were scaled to [0 1] and converted into an 11 by 6 matrix before putting into the models. The experimental reconstruction results are demonstrated in Table 5.

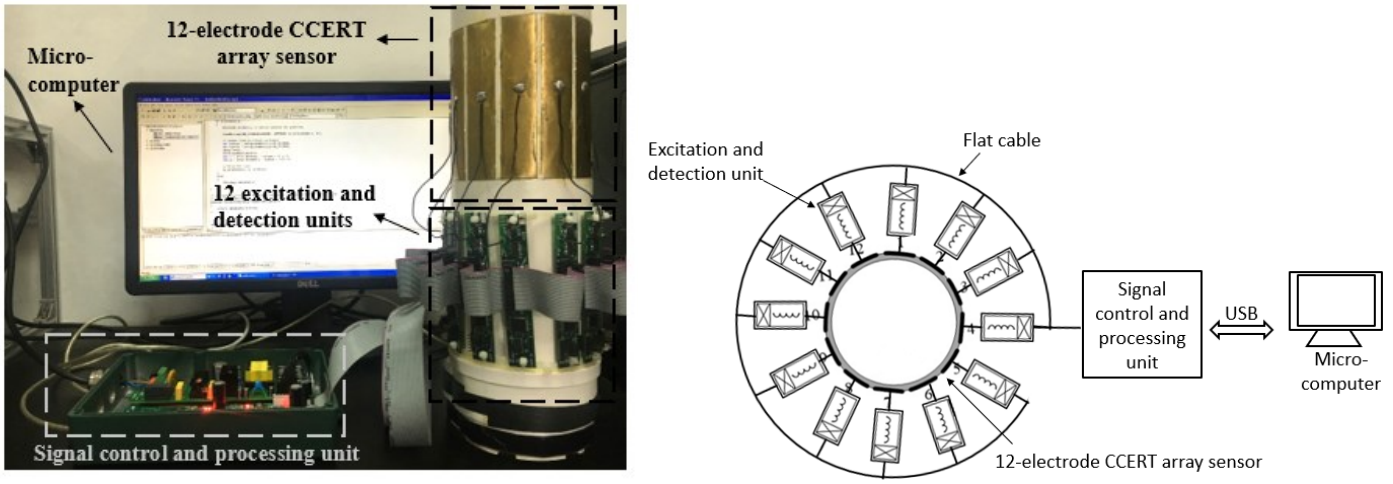

(a) (b)

Figure 9. (a) A photo of the 12-electrode CCERT system. (b) 12-electrode CCERT system setup.

Table 5. Experimental reconstruction results and accuracy analyses.

Case	Image Reconstruction Illustrations	Evaluation Metrics		
1	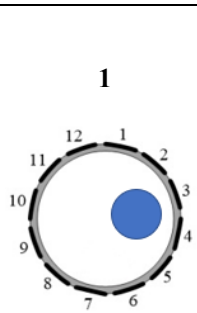 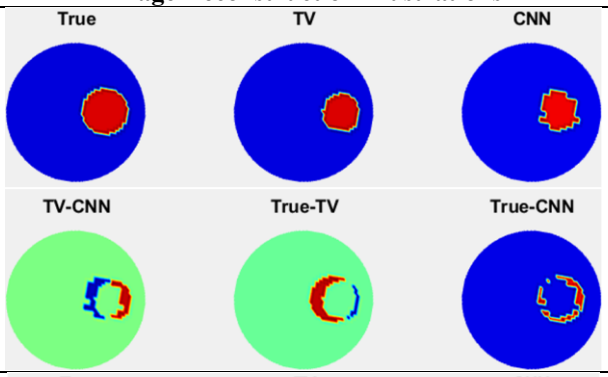	SSIM	CNN	0.8509
			TV	0.8300
			TV-CNN	0.8224
		MSE	CNN	0.0264
			TV	0.0392
			TV-CNN	0.0400
		PSNR	CNN	15.7840
			TV	14.0671
			TV-CNN	13.9794
2	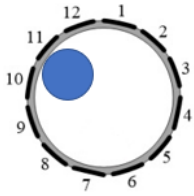 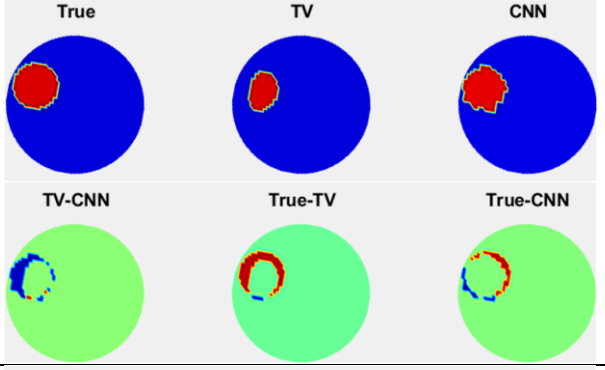	SSIM	CNN	0.8599
			TV	0.8357
			TV-CNN	0.8729
		MSE	CNN	0.0240
			TV	0.0408
			TV-CNN	0.0320
		PSNR	CNN	16.1979
			TV	13.8934
			TV-CNN	14.9485
3	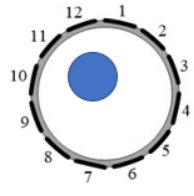 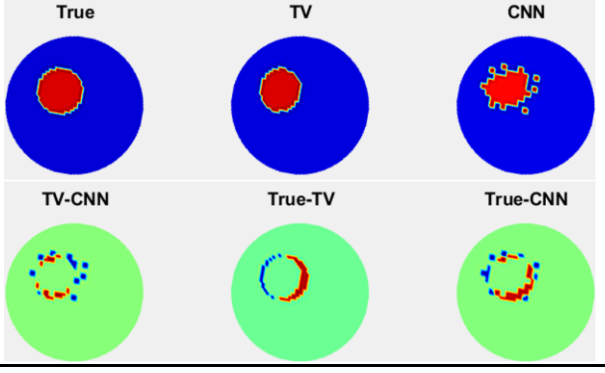	SSIM	CNN	0.8071
			TV	0.8531
			TV-CNN	0.8226
		MSE	CNN	0.0352
			TV	0.0260
			TV-CNN	0.0268
		PSNR	CNN	14.5346
			TV	15.8503
			TV-CNN	15.7187

4	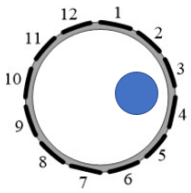	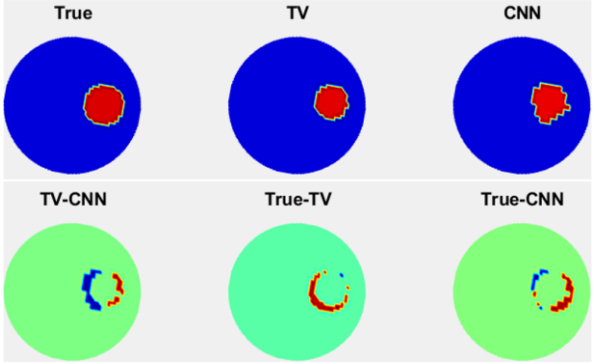	SSIM	CNN 0.8778 TV 0.8879 TV-CNN 0.8581
			MSE	CNN 0.0216 TV 0.0204 TV-CNN 0.0268
			PSNR	CNN 16.6555 TV 16.9037 TV-CNN 15.7187
5	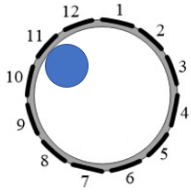	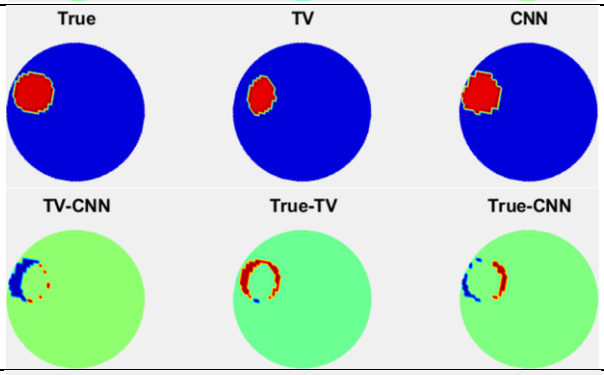	SSIM	CNN 0.8937 TV 0.8708 TV-CNN 0.9000
			MSE	CNN 0.0200 TV 0.0268 TV-CNN 0.0284
			PSNR	CNN 16.9897 TV 15.7187 TV-CNN 15.4668
6	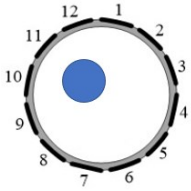	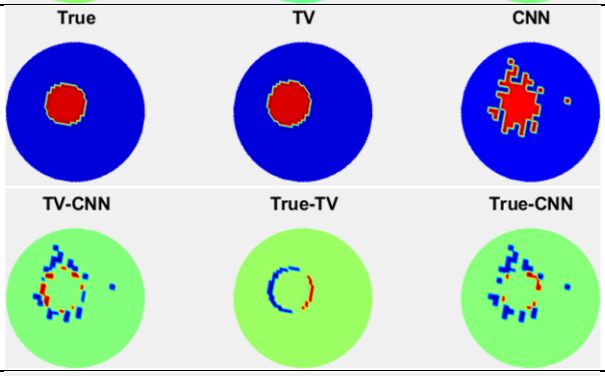	SSIM	CNN 0.7317 TV 0.8679 TV-CNN 0.7244
			MSE	CNN 0.0464 TV 0.0200 TV-CNN 0.0464
			PSNR	CNN 13.3348 TV 16.9897 TV-CNN 13.3348
7		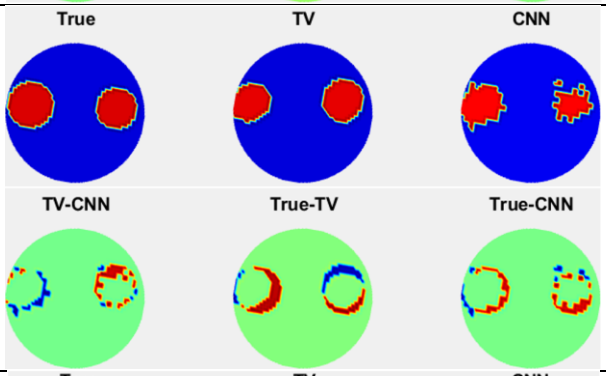	SSIM	CNN 0.6939 TV 0.6830 TV-CNN 0.7469
			MSE	CNN 0.0580 TV 0.0700 TV-CNN 0.0472
			PSNR	CNN 12.3657 TV 11.5490 TV-CNN 13.2606
8		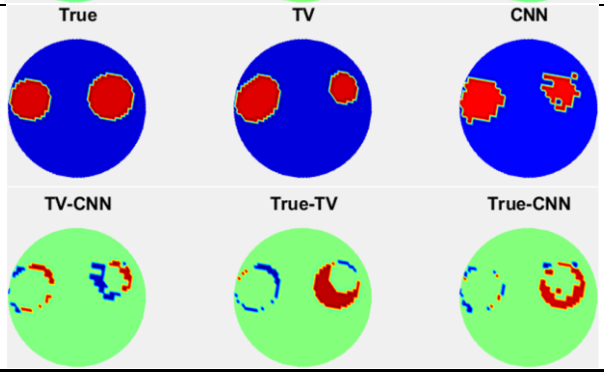	SSIM	CNN 0.7415 TV 0.7236 TV-CNN 0.7440
			MSE	CNN 0.0576 TV 0.0696 TV-CNN 0.0496
			PSNR	CNN 12.3958 TV 11.5739 TV-CNN 13.0452

9 	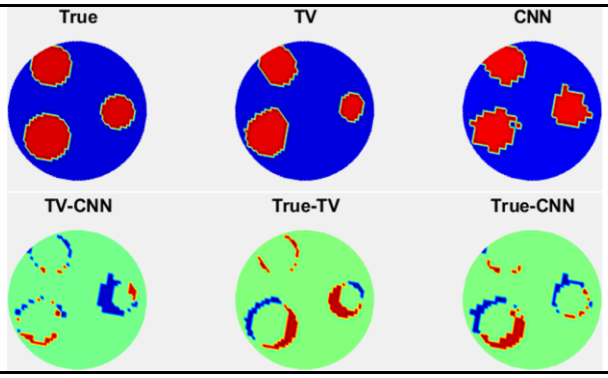	SSIM	CNN	0.6037
			TV	0.6000
			TV-CNN	0.6500
		MSE	CNN	0.0776
			TV	0.0792
			TV-CNN	0.0664
		PSNR	CNN	11.1014
			TV	11.0127
			TV-CNN	11.7783

Comparing Table 4 and Table 5, for each case, the SNR value by CNN for experimental reconstruction is lower than that of the simulation reconstruction due to the random noise and interference during measurements. Besides, the effect of scaling also amplifies the differences. Take the case No.1 as an example, Figure 10 plots the 66 scaled resistance data of simulation and experimental test. Both reasons lead to the decrease of SSIM and increase of MSE in practical reconstruction. Even so, Table 5 shows that CNN can be well applied for the real data to reveal the relative size and position of the plastic rods with average SSIM of 0.7846, average MSE of 0.0408, and average PSNR of 14.3733, which indicates that our networks do well in noise-tolerance. The average SSIM, MSE, and PSNR for TV method is 0.7947, 0.0436, and 14.1732 respectively. Figure 11a, 11b and 11c show the comparisons of SSIM, MSE, PSNR values via CNN and TV.

In all 9 experimental cases, 6 cases have higher SSIM values, lower MSE values and higher PSNR values with CNN method than those with TV algorithm, which demonstrates the improvement in image reconstruction accuracy for CCERT system by multi-CNNs approach and the feasibility of applying deep learning for the two-phase material imaging by CCERT. What's more, the typical calculation time to reconstruct the image with the 625 DL models is around 1 minute. Though the time of producing one image with CNN is longer than that with TV algorithm (several seconds) at the current time, the improvement of GPU in the future can accelerate the reconstruction process to provide the real-time imaging.

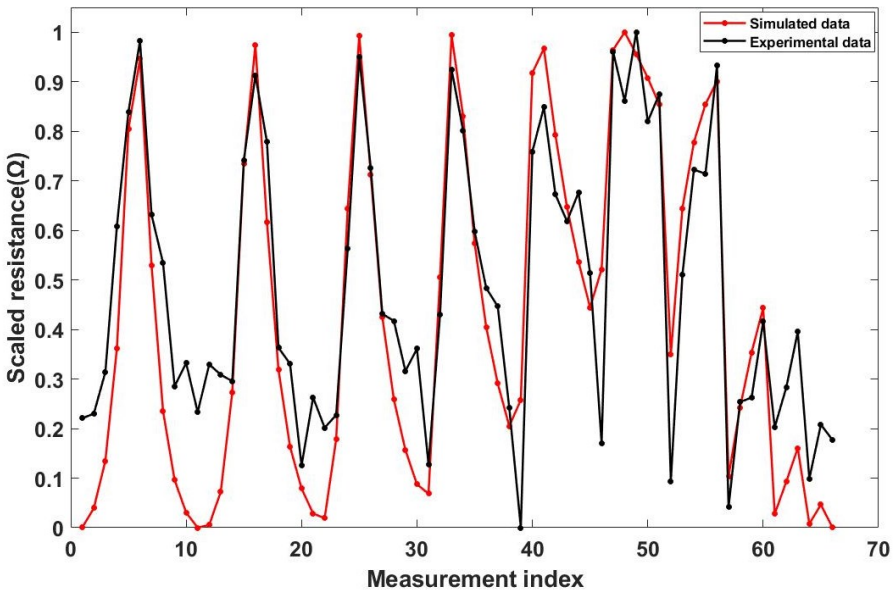

Figure 10. Simulated and experimental resistance plot for case 1.

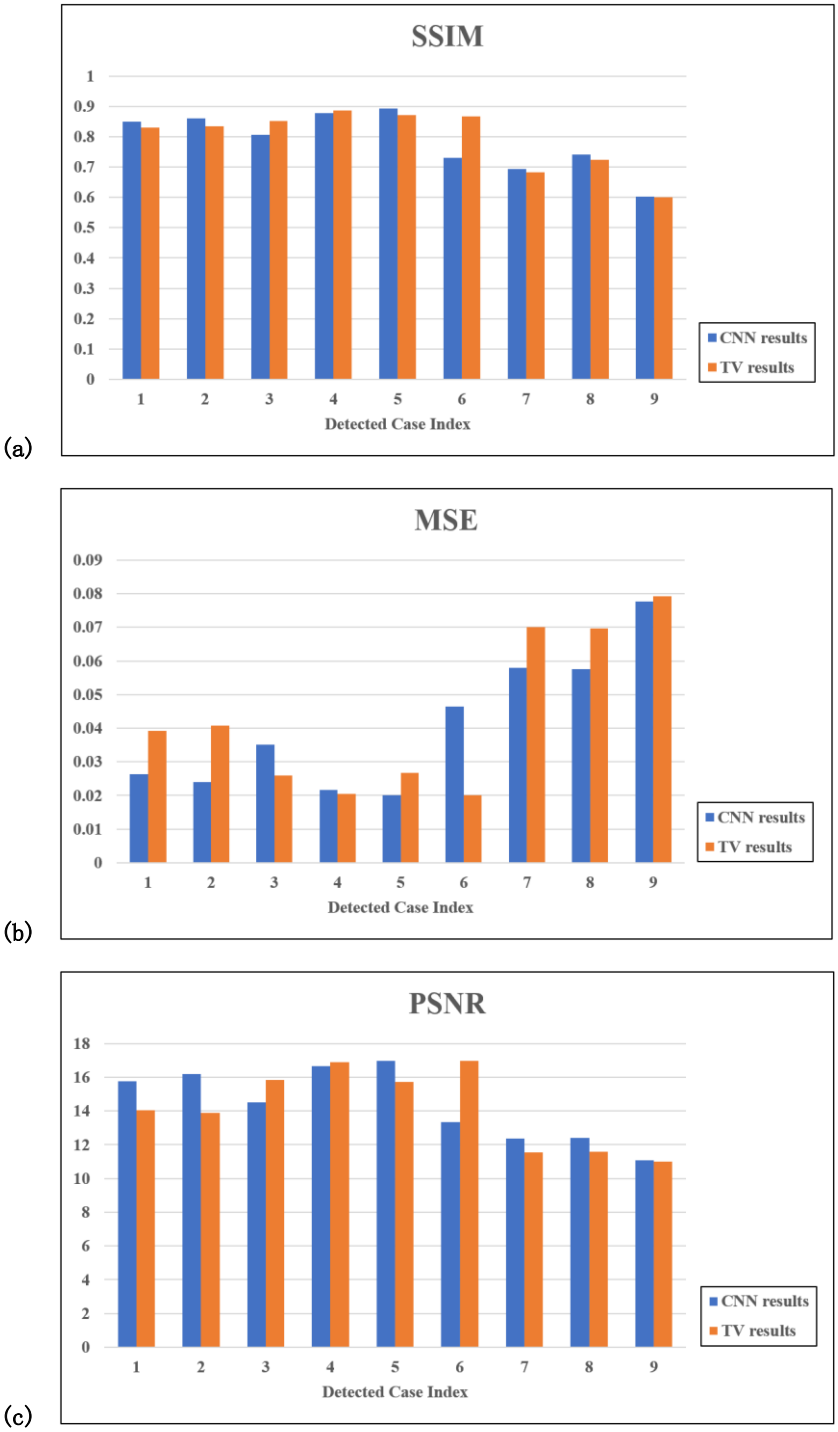

Figure 11. (a) SSIM plot (b) MSE plot (c) PSNR plot for 9 reconstruction cases by CNN and TV.

4. Conclusions

This research studied the feasibility of CNN-based reconstructing algorithm for circular CCERT system. CCERT has the same advantages as the traditional ERT system including simplicity, no invasions, no radiation, rapid response and low cost. Additionally, CCERT avoids contact errors by inserting an insulation layer between the conductive mediums and electrodes. Also, CCERT could achieve higher image quality due to the extended frequency range. The forward model was simulated based on the Maxwell equations and FEM method, and the image reconstruction was realized by a deep learning

approach. CNN was adopted as the network architecture due to its superior ability to extract features from the input data, thereby it's suitable to use CNN for classification tasks. Each 2500-pixel image was divided into 625 clusters so that CNN can be applied on each cluster to solve the distinct multi-class classification problems. Each CNN took in data and mapped into a label representing the pixel distribution. The CNN models were achieved by accessing data, constructing layers, setting training options and conducting training. The training of each CNN was carried on separately to pursue a fitting model for each cluster. After tunings, the 625 models could achieve satisfying training accuracy, and they were then applied for the reconstructions of an entire image. Both simulation images and practical measurement images achieved acceptable results, which confirmed the practicability of applying multiple CNNs for image reconstruction of circular CCERT. Training with the simulated data and successful tests conducted with experimental data are very promising, the result allows greater depth of computer-based optimization of CCERT system. In this study, the CNN approach was compared with one of the state-of-the-art total variation algorithms and provides similar performances. The TV algorithm still needed thresholding of the final image, which is not always straightforward, while CNN is directly producing binary images. In this work, we considered 9 scenarios to test whether the proposed CNN is capable of imaging with high quality. It is worth noticing good performances shown by the state of the art traditional imaging method such as TV algorithm as well as both shallow and deep neural network. In future work, as more scenarios are considered to train the system, such as the case when inclusions contact each other, the performance of the system will become better. In theory the proposed method should handle such nonlinearity but need to be compared with a nonlinear traditional algorithm.

Author Contributions: Methodology and initial idea, G.M., Y.J., M.S.; software development and analysis, G.M and Z.C.; supervision, M.S., B.W..; validation, M.S., B.W., Y.J..; data collection: Y.J..; writing, G.M. and Z.C., read and reviewed by M.S., B.W. and Y.J. All authors have read and agreed to the published version of the manuscript.

Funding: GM's work is supported by University of Bath's Alumni office by Raoul and Catherine Hughes.

Conflicts of Interest: The authors declare no conflict of interest.

References

1. Barber, D.C.; Brown, B.H., Applied potential tomography. *Journal of Physics E: Scientific Instruments*, **1984**, 17, 723.
2. Brown, B.H.; Barber, D.C.; Seagar, A.D., Applied potential tomography: possible clinical applications. *Clinical Physics and Physiological Measurement*, **1985**, 6, 109.
3. Holder, D.S., Electrical impedance tomography (EIT) of brain function. *Brain topography*, **1992**, 5, 87-93.
4. Adler, A.; Arnold, J.H.; Bayford, R.; Borsic, A.; Brown, B.; Dixon, P.; Faes, T.J.; Frerichs, I.; Gagnon, H.; Gärber, Y.; Grychtol, B., GREIT: a unified approach to 2D linear EIT reconstruction of lung images. *Physiological measurement*, **2009**, 30, S35.
5. Cho, K.H.; Kim, S.; Lee, Y.J., A fast EIT image reconstruction method for the two-phase flow visualization. *International communications in heat and mass transfer*, **1999**, 26, 637-646.
6. Brown, B.H. Medical Impedance Tomography and Process Impedance Tomography: A Brief Review. *Meas. Sci. Technol.* **2001**, 12, 991-996.
7. Webster, J.; Adler, A.; Boyle, A. Electrical Impedance Tomography. Wiley Online Library, 2020.
8. Wahaba, Y. A.; Rahimb, R. A.; Rahimanc, M. H. F. Non-invasive Process Tomography in Chemical Mixtures—A Review. *Sensors and Actuators B: Chemical.* **2015**, 210, 602-617.
9. York, T. A. Status of Electrical Tomography in Industrial Applications. *Journel of Electronic Imgaing*, **2001**, 10, 608-619.
10. Boyle, A.; Adler, A. The Impact of Electrode Area, Contact Impedance and Boundary Shape on EIT Images. *Physiological Measurement*, **2011**, 32, 745-754.
11. Jiang, Y.; Soleimani, M. Capacitively Coupled Resistivity Imaging for Biomaterial and Biomedical Applications. *IEEE Access,* **2018**, 6.
12. Wang, B.; Tan, W.; Huang, Z.; Ji, H.; Li, H. Image Reconstruction Algorithm for Capacitively Coupled Electrical Resistance Tomography. *Flow Measurement and Instrumentation,* **2014**, 40, 216-222.

13. Wang, B.; Hu, Y.; Ji, H.; Huang, Z.; Li, H. A Novel Electrical Resistance Tomography System Based on C4D Technique. In Instrumentation and Measurement Technology Conference, IEEE, 2012.
14. Wang, B.; Zhang, W.; Huang, Z.; Ji, H.; Li, H. Modeling and Optimal Design of Sensor for Capcacitively Coupled Electrical Resistance Tomography System. *Flow Measurement and Instrumentation*. **2013**, 31, 3-9.
15. Jiang, Y.; Soleimani, M. Capacitively Coupled Phase-based Dielectric Spectroscopy Tomography. *Scientific Reports.* **2018**, 8.
16. Ma G.; Soleimani, M. Spectral Capacitively Coupled Electrical Resistivity Tomography for Breast Cancer Detection. *IEEE Access,* **2020**, 8.
17. Wang, Y.; Wang, B.; Huang, Z.; Ji, H.; Li, H. New Capacitively Coupled Electrical Resistance Tomography (CCERT) System. *Measurement Science and Techonology*. **2018**, 29.
18. Jiang, Y.; Soleimani, M. Capacitively Coupled Electrical Impedance Tomography for Brain Imaging. *IEEE Transactions on Medical Imaging,*. **2019**, 38.
19. Tan, C.; Lv, S.; Dong, F.; Takei, M. Image Reconstruction Based on Convolutional Neural Network for Electrical Resistance Tomography. *IEEE Sensors Journal*. **2019**, 19, 196-204.
20. Deng, L.; Yu, D. Deep Learning: Methods and Applications, Foundations and Trends in Signal Processing, 2014.
21. Hahnlosor, R. H.; R, S.; Mahowald, M. A.; Douglas, R. J.; Seung, H. S. Digital Selection and Analogue Amplification Coexist in a Cortex-inspired Silicon Circuit. *Nature.* **2000**, 405, 947-951.
22. Glorot, X.; Bordes, A.; Bengio, Y. Deep Sparse Rectifier Neural Networks. In Processings of the Fourteenth International Conference on Artificial Intelligence and Statistics, (AISTATS), 2011.
23. Lucas, A.; lliadis, M.; Molina R.; Katsaggelos, A. Using Deep Neural Networks for Inverse Porblems in Imaging: Beyond Analytical Methods. *IEEE Signal Processing Magazine.* 2018, 35, 20-36.
24. FLOYDHUB. Colorizing and Restoring Old Images and Videos with Deep Learning. *Humans of Machine Learning,* 2018.
25. Fan, Y.; Ying, L. Solving Electrical Impedance Tomography with Deep Learning. *Journal of Computational Physics,* 2020, 404.
26. Li, H.; Schwab, J.; Antholzer S.; Haltmeier, M. NETT: Solving Inverse Problems with Deep Neural Networks. *IOP Science.* **2020**, 36.
27. Amjad, J.; Sokolic, J.; Rodrigues, M. R. On Deep Learning for Inverse Problems. In 26th European Signal Processing Conference (EUSIPCO), 2018.
28. Aghdam, H.; Hamed; Heravi, J.; Elnaz, Guide to Convolutional Neural Networks, Springer, 2017.
29. Wei, Z.; Chen, X., Induced-current learning method for nonlinear reconstructions in electrical impedance tomography. *IEEE transactions on medical imaging*, **2019**, 39, 1326-1334.
30. Zheng, J.; Ma, H.; Peng, L. A CNN-Based Image Reconstruction for Electrical Capacitance Tomography. In 2019 IEEE International Conference on Imaging Systems and Techniques (IST), Abu Dhabi, 2019.
31. Xiao, J.; Liu, Z.; Zhao, P.; Ji, Y.; Huo, J. Deep Learning Image Reconstruction Simulation for Electromagnetic Tomography. *IEEE Sensors Journal.* **2018**, 18.
32. Fernández-Fuentes, X.; Mera, D.; Gómez, A.; Vidal-Franco, I., Towards a fast and accurate eit inverse problem solver: a machine learning approach. *Electronics*, **2018**, 7, 422.
33. Rymarczyk, T.; Kłosowski, G.; Kozłowski, E.; Tchórzewski, P., Comparison of selected machine learning algorithms for industrial electrical tomography. *Sensors*, **2019**, 19, 1521.
34. Tholin-Chittenden, C.; Soleimani, M. Planar Array Capacitive Imaging Sensor Design Optimization. *IEEE Sensors Journal.* **2017**, 17.
35. Li, F.; Soleimani, M.; Abascal, J. Planar Array Magnetic Induction Tomography Further Improvement. *Sensor Review.* **2019**, 39, 257-268.
36. Wang, Y. Study on Image Reconstruction of Capacitively Coupled Electrical Impedance Tomography (CCEIT). *Measurement Science and Techonology,* **2019**, 30.
37. Tan, W., Wang, B., Huang, Z., Ji, H.; Li, H. New image reconstruction algorithm for capacitively coupled electrical resistance tomography. *IEEE Sensors Journal*. **2017**. 17, 8234-8241.
38. Russell, S. J.; Norvig, P. Artificial Intelligence: A Modern Approach(Third ed.), Prentice Hall, 2010.
39. Ndajah, P.; Kikuchi, H.; Yukawa, M.; Watanabe, H.; Muramatsu, S., SSIM image quality metric for denoised images. In Proc. 3rd WSEAS Int. Conf. on Visualization, Imaging and Simulation (pp. 53-58), 2010, November.
40. Sara, U.; Akter, M.; Uddin, M.S., Image quality assessment through FSIM, SSIM, MSE and PSNR—a comparative study. *Journal of Computer and Communications*, **2019**, 7, 8-18.